On the Utility of Individual Tendency Output: Revealing Interactions between Parameterized Processes during a Marine Cold Air Outbreak

MARVIN KÄHNERT,[a,b] HARALD SODEMANN,[a,b] WIM C. DE ROOY,[c] AND TERESA M. VALKONEN[d]

[a] *University of Bergen, Geophysical Institute, Bergen, Norway*
[b] *Bjerknes Centre for Climate Research, Bergen, Norway*
[c] *Royal Netherlands Meteorological Institute (KNMI), De Bilt, Netherlands*
[d] *Development Centre for Weather Forecasting, Norwegian Meteorological Institute, Oslo, Norway*

(Manuscript received 9 February 2021, in final form 30 August 2021)

ABSTRACT: Forecasts of marine cold air outbreaks critically rely on the interplay of multiple parameterization schemes to represent subgrid-scale processes, including shallow convection, turbulence, and microphysics. Even though such an interplay has been recognized to contribute to forecast uncertainty, a quantification of this interplay is still missing. Here, we investigate the tendencies of temperature and specific humidity contributed by individual parameterization schemes in the operational weather prediction model AROME-Arctic. From a case study of an extensive marine cold air outbreak over the Nordic seas, we find that the type of planetary boundary layer assigned by the model algorithm modulates the contribution of individual schemes and affects the interactions between different schemes. In addition, we demonstrate the sensitivity of these interactions to an increase or decrease in the strength of the parameterized shallow convection. The individual tendencies from several parameterizations can thereby compensate each other, sometimes resulting in a small residual. In some instances this residual remains nearly unchanged between the sensitivity experiments, even though some individual tendencies differ by up to an order of magnitude. Using the individual tendency output, we can characterize the subgrid-scale as well as grid-scale responses of the model and trace them back to their underlying causes. We thereby highlight the utility of individual tendency output for understanding process-related differences between model runs with varying physical configurations and for the continued development of numerical weather prediction models.

SIGNIFICANCE STATEMENT: Accurately capturing the evolution of the lower atmosphere with weather models in use at national forecasting centers requires the representation of processes from millimeter to subkilometer scale. Examples are the formation of water droplets within clouds or the transport of heat by turbulent swirls. All of these processes are represented by simplified formulations that introduce uncertainty into models. In this study, we employ a new diagnostic in the forecast model AROME-Arctic to investigate the contributions of these simplified processes. We identify regimes that foster distinct contributions to the heat and humidity profiles from individual processes, allowing us to explain changes to the modeled temperatures or vertical velocity. Knowledge of these regimes aids in the interpretation of the output from weather models, highlighting the benefit of our diagnostics for researchers and weather forecasters.

KEYWORDS: Diagnostics; Mesoscale models; Numerical weather prediction/forecasting; Parameterization; Subgrid-scale processes

1. Introduction

High-impact weather events in the Arctic, such as maritime icing, severe snow showers, and polar lows, are often linked to marine cold air outbreaks (mCAO; Businger and Reed 1989; Papritz and Pfahl 2016; Samuelsen and Graversen 2019). During an mCAO, cold and dry air is advected over warmer waters. The resulting strong air–sea temperature contrasts give rise to intense sensible and latent heat fluxes that have been observed to exceed 1000 W m^{-2} (Grossman and Betts 1990). Such heat fluxes transform the formerly cold, dry, and stably stratified air masses into warmer, more humid, and unstable air masses, giving rise to pronounced convective mixing and cloud formation (Etling and Brown 1993; Hartmann et al. 1997). Heavy precipitation can therefore result downstream of an mCAO and affect the population and infrastructure in coastal regions. Adequately forecasting mCAOs is thus an important task for operational weather forecasting centers.

Yet, numerical weather prediction (NWP) models often struggle to accurately forecast mCAOs (Field et al. 2017; Abel et al. 2017). Prominent challenges include forecasting the rapid growth of the boundary layer, the development

Denotes content that is immediately available upon publication as open access.

Supplemental information related to this paper is available at the Journals Online website: https://doi.org/10.1175/WAF-D-21-0014.s1.

Corresponding author: Marvin Kähnert, marvin.kahnert@uib.no

DOI: 10.1175/WAF-D-21-0014.1

and composition of boundary layer clouds, and the transition in cloud cover during an mCAO. All of these characteristics involve microscale and mesoscale processes that in turn rely on the accurate calculation of subgrid-scale processes, such as turbulent fluxes and cloud microphysical variables.

Due to the limited resolution in current NWP models, the effect of subgrid-scale processes is represented by parameterization schemes, including the turbulence scheme, shallow convection scheme, and microphysics scheme. At high latitudes, where mCAOs are prevalent, these schemes are often poorly constrained (Morrison et al. 2012; Vihma et al. 2014), while some even reach their limits of applicability, such as the shallow convection scheme (Honnert et al. 2011; Holloway et al. 2014). The spectrum of convective length scales during an mCAO cannot be fully represented by the kilometer-scale grid spacing of current operational NWP models. Therefore, difficulties emerge to define a proper partitioning between the amount of resolved and parameterized vertical transport. These difficulties can lead to an overrepresentation of parameterized vertical transport in the model and therefore to model error (e.g., Honnert et al. 2011).

Thus, the accuracy of an mCAO simulation critically depends on the interplay between resolved scales and the contribution from several physical parameterization schemes that each have specific limitations. Even though this interplay has been recognized to contribute to forecast uncertainty (Vihma et al. 2014; Field et al. 2014; Abel et al. 2017), a quantification of this interplay is so far lacking.

To quantify the interplay of parameterized physical processes, and to assess their contributions to the model state, we implement here the output of the physical tendencies contributed by individual parameterizations, termed *individual tendency output*, in an operational NWP model. We use the operational, limited-area NWP model AROME-Arctic (Müller et al. 2017b) and focus our analysis on physical tendencies for temperature and specific humidity. A major mCAO in 2015, studied by Papritz and Sodemann (2018), which impacted a particularly large fraction of the Nordic seas (and also the model domain) forms our case study. Using the individual tendency output, we study the interplay between resolved and parameterized processes, and assess the sensitivity of this interplay to changes in the model's physical parameterizations.

2. Model description and methods

a. AROME-Arctic

AROME-Arctic is an operational, convection-permitting forecasting system covering the European Arctic (Fig. 1). The base NWP model used for AROME-Arctic, and for the implementation of the individual tendency output is HARMONIE-AROME cycle 40h1.1 (Bengtsson et al. 2017). In the current configuration, the model has a horizontal grid spacing of 2.5 km, 65 vertical hybrid sigma-pressure coordinates reaching up to 9 hPa (24 km), and a semi-Lagrangian spectral advection scheme. The model contains a wide range of advanced physical

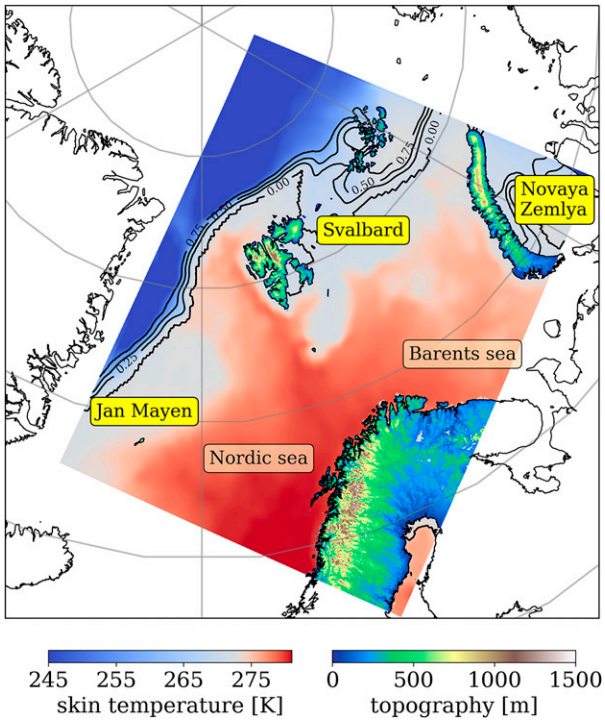

FIG. 1. The domain of the AROME-Arctic model. The shading over land indicates model topography, and the shading over water indicates skin temperature (K) from the control run (REF). Areas colder than 273 K are covered by sea ice. The skin temperature over water remains unchanged throughout the model run. The black contours indicate sea ice cover.

parameterization schemes, including cloud microphysics, radiation, surface processes, shallow convection, and turbulence, as detailed in the following.

The microphysics scheme (OCND2; Müller et al. 2017a) consists of three steps. First, during the microphysical adjustment step, thermodynamic equilibrium is enforced between the microphysical species and the temperature field. In the second step, the scheme calculates six prognostic variables: water vapor, cloud water, rain, ice, snow, and graupel. OCND2 thereby takes sublimation, evaporation, and interactions between species into account. Finally, the three-dimensional cloud fraction is diagnosed by a statistical cloud and condensation scheme (Bougeault 1982; Bechtold et al. 1995). OCND2 provides physical tendencies for water vapor, all hydrometeor species, and temperature.

The radiation scheme (RRTM; Fouquart and Bonnel 1980; Mlawer et al. 1997) provides radiative fluxes as input to the surface scheme and to the column temperatures. Shortwave radiation is computed using six spectral bands, while the longwave radiation is calculated by utilizing climatological distributions of aerosols and ozone. RRTM provides physical tendencies for temperature.

The surface scheme (SURFEX; Le Moigne 2009) provides sensible and latent heat fluxes as well as wind stress which are used by the turbulence and shallow convection scheme. SURFEX separates a grid box into four tiles (sea, lakes,

TABLE 1. Individual tendencies for temperature T and specific humidity R in the AROME-Arctic model utilized in this study.

Tendency	Scheme	Reference(s)
δT^{phys}, δR^{phys}	Total physical tendency, sum of all individual schemes	—
δT^{dyn}, δR^{dyn}	Dynamical tendency comprising the contributions from the model dynamics and the horizontal diffusion scheme	—
δT^{adj}, δR^{adj}	Thermodynamical adjustment step from microphysics	Müller et al. (2017a)
δT^{micro}, δR^{micro}	Cloud microphysics scheme, OCND2	Müller et al. (2017a)
δT^{turb}, δR^{turb}	TKE-turbulence scheme, HARATU	Lenderink and Holtslag (2004), Bengtsson et al. (2017)
δT^{sc}, δR^{sc}	Dual-updraft, shallow convection scheme	de Rooy and Siebesma (2008), Neggers et al. (2009)
δT^{EDMF}, δR^{EDMF}	Eddy-diffusivity mass-flux scheme, sum of turbulence and shallow convection	Soares et al. (2004), Siebesma et al. (2007)
δT^{rad}	Radiation scheme, RRTM	Fouquart and Bonnel (1980), Mlawer et al. (1997)

urban areas, nature), each represented by specific formulations. The total flux in each grid box is summed and weighted by its respective tile fractions. SURFEX further computes quantities like the surface albedo and emissivity which are then used by the radiation scheme. SURFEX does not directly contribute to the tendencies of temperature, moisture, or wind in the atmospheric model, but instead influences the tendencies provided by the boundary layer or the radiation scheme. Consequently, SURFEX does not appear as an individual process in the subsequent tendency analysis.

Finally, the boundary layer scheme is formulated using an eddy-diffusivity mass-flux framework (EDMF; Soares et al. 2004; Siebesma et al. 2007). The EDMF framework consists of two parts. The turbulence (''ED'') part is called HARMONIE-AROME with RACMO Turbulence (HARATU; Lenderink and Holtslag 2004; Bengtsson et al. 2017), and uses a prognostic equation for turbulent kinetic energy (TKE) together with a diagnostic length scale. For stable conditions, a generally accepted form of the length scale depending on the local stability is used (Deardorff 1980; Baas et al. 2008). For near-neutral to unstable conditions, the length scale consists of vertical integrals of stability-dependent functions (Lenderink and Holtslag 2004). The shallow convection part (''MF'') uses a dual updraft framework (Neggers et al. 2009). It distinguishes between dry updrafts that do not experience condensation and stop in close vicinity to the lifting condensation level, and moist updrafts that condense and form clouds. Both updrafts have different entrainment and detrainment rates (de Rooy and Siebesma 2008; Bengtsson et al. 2017; de Rooy et al. 2021, manuscript submitted to *Geosci. Model Dev.*, hereafter DR21). Each part of the EDMF scheme provides a physical tendency for temperature, humidity, and momentum.

The model configuration described above is used in our reference run (REF). REF contains one distinct difference from the operational configuration of AROME-Arctic at the time of this study: snow and rain produced by the shallow convection scheme are treated as resolved precipitation, which serves as input to the microphysics scheme. This setting (named LTOTPREC) is active for every model run discussed in this study. Positive impacts of this setting on mesoscale organization, prominent during an mCAO, have been found in preoperational tests for the model cycle 43 conducted at KNMI. The control run is initialized at 0000 UTC 24 December 2015 and was integrated for 72 h.

b. *Individual tendency output in AROME-Arctic*

We now briefly describe the implementation of individual tendency output as a new diagnostic in AROME-Arctic. A tendency refers to the change of a variable X over time. The absolute change in X between two succeeding time steps dX/dt is often called the total tendency and can be decomposed as follows:

$$\frac{dX}{dt} = D + K + \sum \delta X^i, \tag{1}$$

where D is the tendency due to the model dynamics, K is the tendency due to the horizontal diffusion, and $\sum \delta X^i$ is the sum of all individual physical tendencies, or the *total physical tendency*. The dynamical tendency represents advection, whereas the horizontal diffusion mainly smoothes the model fields to stabilize the dynamical core. In AROME-Arctic, both D and K are spectral computations, whereas the total physical tendency $\sum \delta X^i$ consists of gridpoint computations. Table 1 summarizes all individual tendencies for temperature and specific humidity that are output. In the AROME-Arctic model, the prognostic variables that are provided to the parameterization schemes are not influenced by the tendencies produced in the same time step. Thus, the order in which the schemes are called does not influence the individual tendencies. The only exception is the microphysical adjustment step (see above) that is performed at the very beginning of the physical package (Seity et al. 2011).

While the diagnosis and output of physical tendencies are straightforward, a problem arises for the dynamical and horizontal diffusive tendencies. In HARMONIE-AROME, the respective tendencies of the physical schemes are added to the prognostic variables before the dynamical routines are called (Seity et al. 2011). As a result, identifying the additional contributions coming from either the dynamics or horizontal diffusion within the same model time step, without risking double-counting contributions coming from the model physics, becomes impossible. Therefore, D and K are here obtained as a summed residuum from subtracting the physical tendency from

the total tendency of the previous time step. We call this residuum the *dynamical tendency* throughout this study. All obtained tendencies are Eulerian, accumulated over the hourly output interval of the model and provided at every model grid point and level.

c. Boundary layer–type diagnostics

An mCAO is accompanied by remarkable transformations of air masses, from stably stratified over sea ice–covered areas to a convective boundary layer over open water. The parameterization schemes need to be able to represent the varying characteristics of such differing regimes. For this reason, HARMONIE-AROME cy40.1.1 distinguishes between five planetary boundary layer (PBL) types (Fig. 2): stable PBL (I), dry convective (II), stratocumulus topped (III), shallow cumulus topped (IV), and deep convection (V). We now describe how the PBL types I–V are diagnosed, and how they influence the shallow convection scheme.

In the case of stable conditions, characterized by downward surface buoyancy flux as indicated by the idealized temperature profile (Fig. 2, type I), no convective transport can be expected and the PBL is diagnosed as type I (stable). In case of unstable conditions (Fig. 2, type II–V), convective transport becomes important, and dry and moist updrafts are calculated. These calculations require fractional entrainment rates that depend on the ''inversion height'' (Siebesma et al. 2007; DR21). However, this inversion height is not known a priori. Therefore, a test parcel is released, with an entrainment formulation that does not depend on inversion height, following Neggers et al. (2009) and Neggers (2009). The inversion height is determined as the height where the vertical velocity of a dry test parcel becomes 0, or if condensation occurs, set equal to the lifting condensation level. In the case of condensation, furthermore the cloud layer depth is estimated. These variables are subsequently used to distinguish between different convective PBL types.

If the test parcel does not reach the lifting condensation level (LCL; see Fig. 2, type II), the corresponding PBL type is of type II (dry convective) and only dry updrafts (yellow) occur. If the test parcel reaches the LCL, the PBL type is of type IV (shallow cumulus), and moist updrafts (blue) are possible. A further distinction is made if a strong inversion occurs (Fig. 2, type III) and $\theta_{700\text{hPa}} - \theta_{\text{surf}} > 20$ K (Klein and Hartmann 1993). In this case, the PBL type is set to type III (stratocumulus). With PBL type III, only moist updrafts occur, whereas both moist and dry updrafts occur with type IV. Finally, if the test parcel diagnoses a cloud layer depth that exceeds 4000 m, the PBL type is set to type V (deep convection). PBL type V

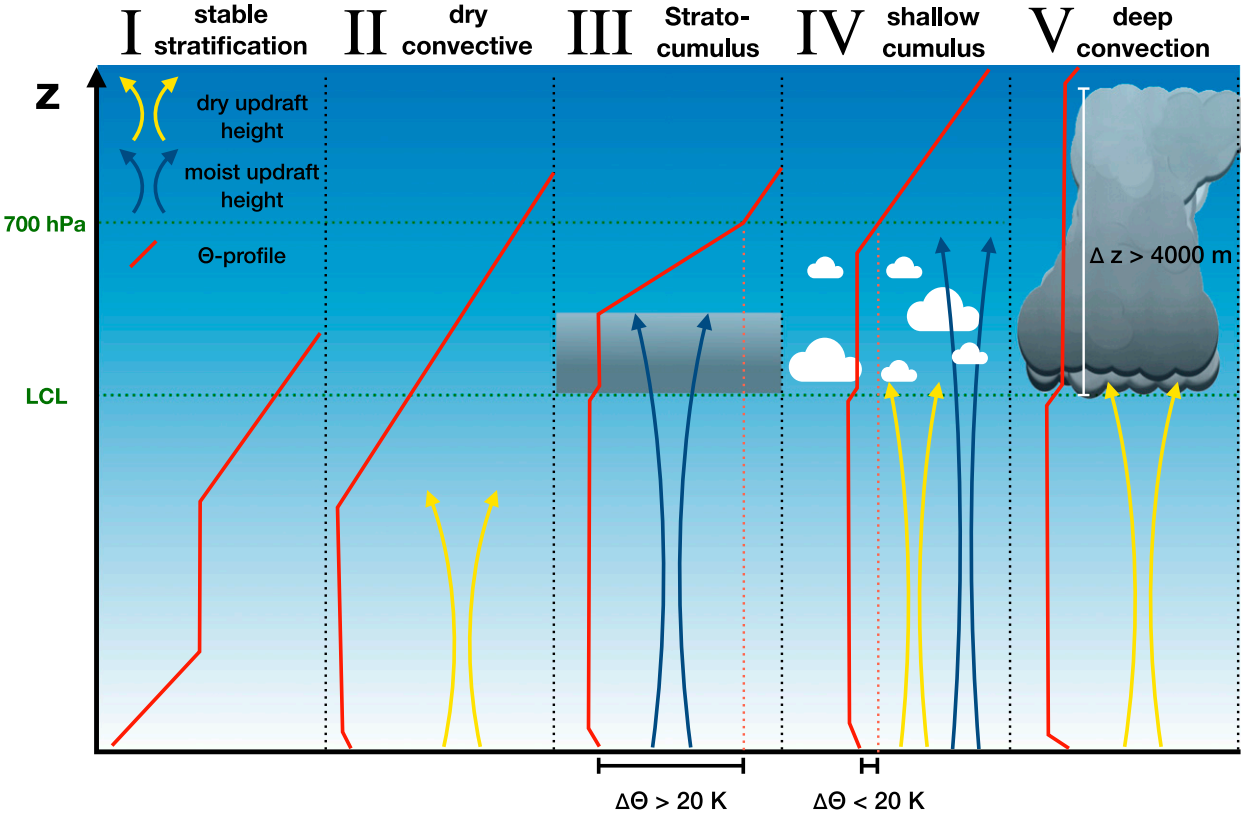

FIG. 2. Schematic showing the boundary layer types in HARMONIE-AROME and their implications for the shallow convection scheme. Idealized potential temperature profiles are shown in red. Yellow and blue arrows depict idealized dry and moist updrafts. The red stippled lines in III and IV indicate the differentiation criteria of Klein and Hartmann (1993). The green stippled lines indicate the lifting condensation level (LCL) and the 700-hPa level, respectively.

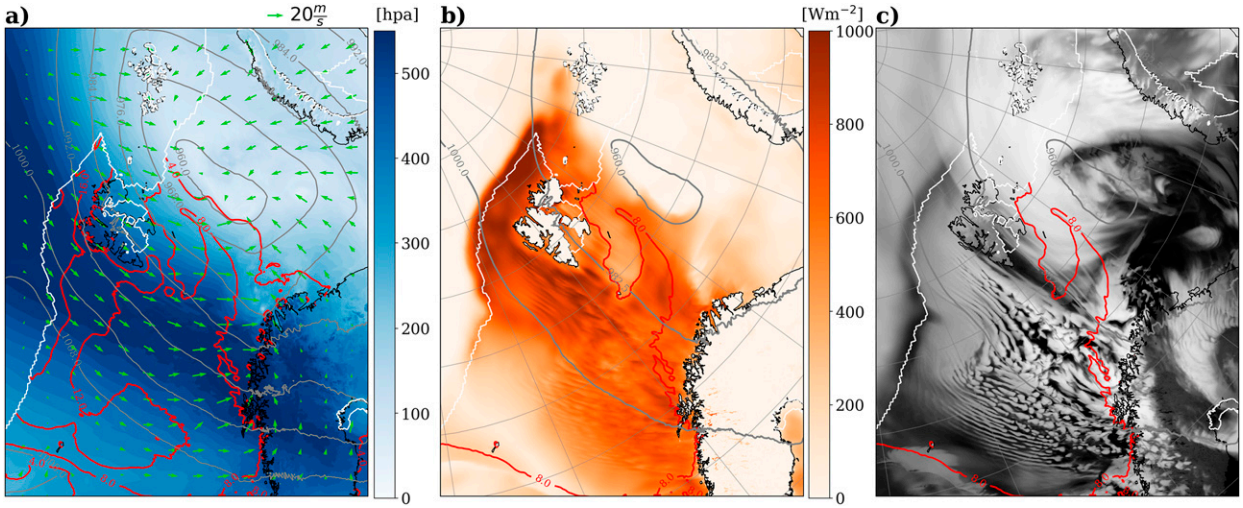

FIG. 3. Synoptic snapshots of the modeled marine cold air outbreak at 1200 UTC 26 Dec 2015 from the control run REF. (a) Thickness of the layer below the 280-K isentropic surface (cold air mass; hPa; blue shading), the CAO index ($\theta_{SST} - \theta_{900}$; K; red contour), the mean sea level pressure (hPa; gray contours), the 10-m winds (m s^{-1}; green arrows). (b) The sum of sensible and latent heat fluxes (W m^{-2}). (c) The top of the atmosphere outgoing longwave radiation as a proxy for cloud cover. Selected pressure contours (gray) in (b) and (c) indicate the prevalent surface trough, while the 8-K contour of the CAO index (red) indicate regions strongly affected by the mCAO. The sea ice edge is depicted in white.

assumes that the model resolves moist convection, and only dry convection remains parameterized.

The diagnosed PBL types directly influence the shallow convection scheme, and can also influence other parameterization schemes through various interplay. In our further analyses, we, therefore, need to consider these PBL types when investigating the behavior of individual tendencies.

d. *The sensitivity experiments*

To put the observed interplay of different parameterization schemes during the mCAO into perspective, we conduct two sensitivity experiments with altered model physics. Like REF, each experiment has a runtime of 72 h and starts at 0000 UTC 24 December 2015. Throughout this study, these experiments are referred to as NOSH and NEW, with the respective details given below.

For the sensitivity experiment NOSH, the shallow convection scheme is deactivated, impacting the partitioning between resolved and parameterized vertical transport. Changing this partitioning has profound impacts on the development of atmospheric profiles and boundary layer clouds during an mCAO in other model studies (Field et al. 2017; Tomassini et al. 2017).

Sensitivity experiment NEW contains several extensive changes to the physics that are being considered for future model versions (DR21). A thoroughly revised statistical cloud scheme is used. As a result of substantial modifications to the turbulence scheme, atmospheric inversions are better preserved. An additional TKE source term enables more ventilation between subcloud and cloudy layers by the turbulence scheme. This source term is referred to as the "energy cascade" and is driven by the mass flux. In the convection scheme, the susceptibility of the mass flux toward stronger sensible heat fluxes is increased to better capture the onset of diurnal convection by decreasing near-surface entrainment rates. Unlike NOSH, NEW is characterized by increased activity of the shallow convection scheme. In NEW, the stratocumulus PBL type (type III) has been eliminated.

e. *The marine cold-air-outbreak case study*

For our case study, we select an extensive mCAO event in the Fram Strait that developed on 24 December 2015 and lasted until 27 December 2015. Using water vapor tracers in the Consortium for Small-Scale Modeling (COSMO) model, Papritz and Sodemann (2018) found that this particular mCAO created its own water cycle with local evaporation, pronounced convective overturning in the PBL, and rapid precipitation formation. In addition to this event being exemplary for mCAOs in the Nordic seas, their results indicate a strong influence of the parameterization schemes on the simulation results.

We use two diagnostics to characterize the mCAO: the *CAO index* and the *cold air mass*. The CAO index is defined as the air–sea potential temperature difference between the surface and 900 hPa, allowing for delineation of an mCAO at the surface. The cold air mass describes the volume of air between the ground and a certain isentropic surface [280 K, similar to the average sea surface temperature, Papritz and Sodemann (2018)]. Air masses leaving the sea ice–covered areas while being located below that isentropic surface can contribute to the mCAO (Iwasaki et al. 2014). Provided that the correct isentropic surface is used, the cold air mass captures both the horizontal and vertical extent of the mCAO.

During the event, an extensive surface trough in the Nordic seas (gray contours, Fig. 3a) led to a persistent transport of cold air over the sea ice edge at low levels (green arrows). The CAO index (red contours) frequently exceeds 8 K, indicating a strong event. A dome of cold air (dark blue shading), extending up to 550 hPa, reaches from the sea ice edge (white line) across the Nordic Seas to northern Scandinavia. The emerging

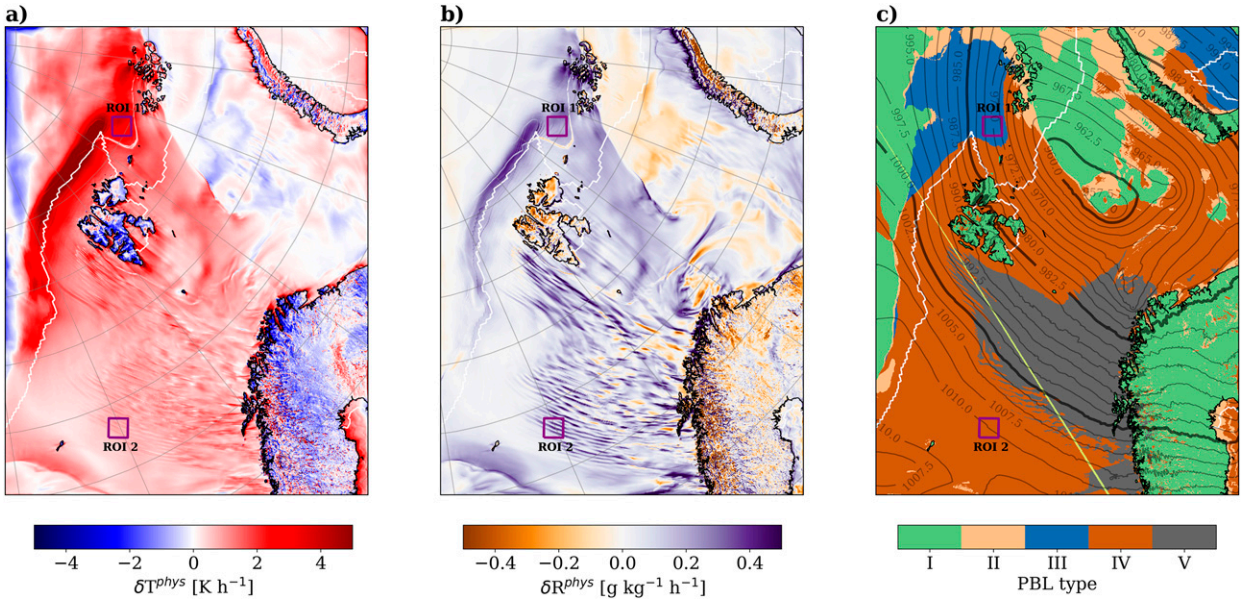

FIG. 4. (a) Physical tendency of temperature δT^{phys} (K h^{-1}) at the lowest model level. (b) Physical tendency of specific humidity δR^{phys} (g kg^{-1} h^{-1}) at the lowest model level. (c) Diagnosed boundary layer types in AROME-Arctic: stable stratification (I), dry convective (II), stratocumulus topped (III), shallow cumulus topped (IV), and deep convection (V). The displayed time is 1200 UTC 25 Dec 2015. Mean sea level pressure (hPa) is in black contours, and the white line indicates the sea ice edge. A north–south cross section (yellow line) is highlighted in (c), as well as two regions of interest (ROI; purple) used in the subsequent analysis in sections 3b and 3c.

gradients of temperature and moisture strongly impact the combined sensible and latent heat fluxes (Fig. 3b; Papritz and Sodemann 2018). Along the sea ice edge, turbulent heat fluxes exceed 1000 W m^{-2}, fueling vertical mixing and leading to extensive growth of the boundary layer (section 3b).

Cloud cover, depicted using outgoing longwave radiation (OLR) at the top of the atmosphere (TOA) as a proxy, shows a dense stratocumulus deck close to the sea ice edge between Svalbard and Jan Mayen (Fig. 3c). The stratocumulus deck breaks into cellular convection farther south over warmer sea surface temperatures, and convective rolls start to appear. We expect that interactions between resolved and subgrid processes are especially active in these regions, making them a focal point in the following investigation.

3. Results

a. *The role of boundary layer types*

First, we examine the total physical tendencies of temperature δT^{phys} and humidity δR^{phys} at the lowest model level. As the total physical tendency incorporates the contributions of every individual parameterization scheme [Eq. (1)], it helps to identify general patterns in the tendency output that might be linked to different interplays between the schemes. Most of the model domain affected by the mCAO (Fig. 3) exhibits positive values of δT^{phys} and δR^{phys} (Figs. 4a,b). Thus, the lowest model level is warmed and moistened by the model physics. This contribution is not uniform across the domain, and distinct spatial patterns emerge. These patterns align with the location of strong sensible heat fluxes (Fig. 3b) or are collocated to model internal PBL types (Fig. 4c).

Strong contributions from δT^{phys} occur along the sea ice edge (Fig. 4a, white line), collocated with the strong turbulent heat fluxes (cf. Fig. 3b). Here, δT^{phys} is largest with values near 5 K h^{-1}. Notably, large contributions occur ahead of the indicated sea ice edge because leads in the marginal ice zone permit high sensible heat fluxes.

An example of the dependency on PBL types exists both west and southwest of Svalbard, where a striped pattern in the physical tendencies is present, in particular for δR^{phys} (Fig. 4b). This pattern originates from partially resolved, mesoscale convection in the form of convective rolls (shown later). This convection occurs with the deep convective PBL type (Fig. 4c, Type V, gray shading), and farther south, also occurs with the shallow convective PBL type (Fig. 4c, Type IV, brown shading).

Cooling and drying predominately occur where the stable PBL type is present (Fig. 4c, Type I, green shading). These regions include all landmasses, parts of the sea ice covered area, and an area west of the Novaya Zemlya archipelago that is not affected by the mCAO.

Northeast of Svalbard, a pattern that resembles a nose emerges. Here, δT^{phys} neither warms nor cools the atmosphere, while all surrounding grid points display warming contributions. In a similar fashion, δR^{phys} exhibits a drying contribution here, while all surrounding grid points exhibit moistening. This pattern coincides with the transition from the stratocumulus (Type III, blue) to the shallow cumulus topped (Type IV, brown) PBL type (Fig. 4c). Thus, model-internal PBL types are important factors in near-surface temperature and moisture tendencies in the AROME-Arctic model.

b. *Tendencies within the mCAO*

To facilitate comparison with the sensitivity runs, we first describe the interplay of individual tendencies within the

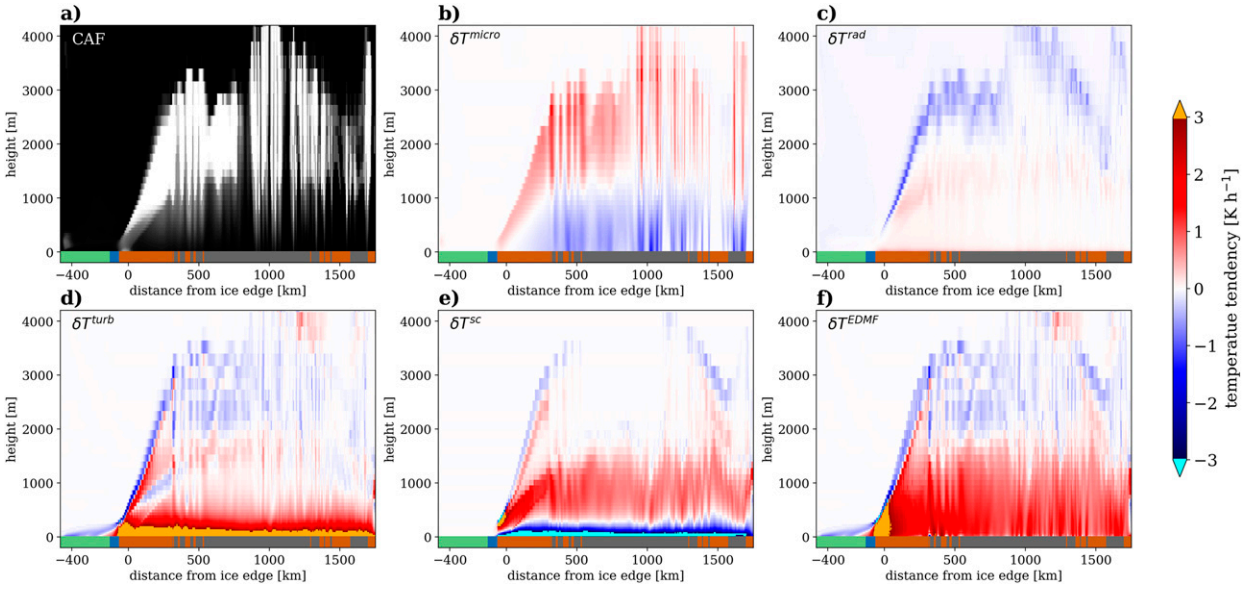

FIG. 5. Cloud area fraction (CAF) and single temperature tendencies along the north–south cross section indicated in Fig. 4c. The abscissa denotes distance from the sea ice edge in km. Ordinate denotes height in m. The panels show (a) CAF (0–1), (b) microphysics tendency δT^{micro} (from −1.5 to 1.8 K h^{-1}), (c) radiation tendency δT^{rad} (from −1.1 to 1.0 K h^{-1}), (d) turbulence tendency δT^{turb} (from −4.6 to 19.0 K h^{-1}), (e) shallow convection tendency δT^{sc} (from −16.5 to 5.6 K h^{-1}), and (f) EDMF-tendency δT^{EDMF} (from −8.6 to 7.1 K h^{-1}). At the bottom of each panel the diagnosed PBL type along the cross section is shown following the shading in Fig. 4c.

mCAO in REF. Throughout the mCAO, the PBL transforms rapidly, as evident from the differences in PBL types. A vertical cross-section, reaching from the stable PBL over sea ice and through the deep convective boundary layer west of Svalbard (Fig. 4c, yellow line) shows the growth of the PBL and individual tendencies within the mCAO (Fig. 5). As depicted by the zero cloud area fraction (CAF), no boundary layer clouds are simulated over most of the sea ice–covered areas (Fig. 5a, negative range of the abscissa). This changes with the onset of the shallow cumulus PBL type close to the sea ice edge. From there southward, boundary layer clouds develop and extend from around 500 to 3500 m. Approximately 400 km away from the sea ice edge, the PBL transitions to deep convective, accompanied by a breakup of cloud cover. This breakup first appears in form of equidistant cloud structures of similar size that emerge from convective rolls (Fig. 3b). Around 1000 km from the sea ice edge, smaller cloud structures emerge due to cellular convection.

The microphysics tendency δT^{micro} is consistently negative, indicating cooling, in all layers below cloud base, while being positive, indicating warming, in the cloud layers (Fig. 5b). The cooling comes from evaporation and sublimation, while the warming comes from condensation, freezing, and deposition (not shown), consistent with Joos and Wernli (2012). The LCL coincides with the transition from negative to positive contributions. The roll clouds and convective cells lead to pronounced warming of up to 3 K h^{-1}, due to increased transport of water vapor into these cloud features and a stronger release of latent heat by condensation and freezing (not shown).

The radiative tendency δT^{rad} displays distinct negative values near the cloud tops (Fig. 5c), caused by the different emissivities present within and above the cloud due to the change in water vapor and hydrometeor content. As the mCAO took place during the polar night, only longwave radiation contributes to δT^{rad}. Consequently, a radiative imbalance forms, locally cooling the atmosphere at about −2 K h^{-1}. Minor radiative warming contributions exist in the lower half of the clouds and near the surface.

We now turn to the turbulence and shallow convection tendencies, δT^{turb} and δT^{sc}. Due to their strong interplay, these two tendencies should be regarded together. The δT^{turb} and δT^{sc} are substantially larger compared to all other contributing tendencies, especially near the surface (Figs. 5d,e). Over the sea ice, where a mix of stable and stratocumulus-topped PBL types is present, δT^{turb} is the only tendency with a notable contribution. In the stable PBL, δT^{turb} is negative, thus the turbulence parameterization cools the shallow PBL. With the onset of the stratocumulus-topped PBL type, small positive contributions of about 1 K h^{-1} appear in the lowest 100 m of the atmosphere. Near the sea ice edge, in the marginal ice zone, a gradual increase in boundary layer height from 30 to 200 m occurs. With the onset of the shallow cumulus PBL type beyond the sea ice edge, the rate of boundary layer deepening rapidly increases. Here, δT^{turb} remains positive throughout most of the PBL, with a warming rate that reaches values of up to 19 K h^{-1} near the surface. At the top of the PBL, this warming diminishes until δT^{turb} becomes negative, and the turbulence parameterization cools the atmosphere because the scheme mixes colder air upward into the inversion layer atop the PBL (Stull 1988).

The shallow convection scheme is inactive in the stable PBL (cf. Fig. 2, type I), and is largely idle in the stratocumulus PBL type (Fig. 5e). With the onset of the shallow cumulus PBL type, δT^{sc} exhibits large negative values up to −16 K h^{-1} in the

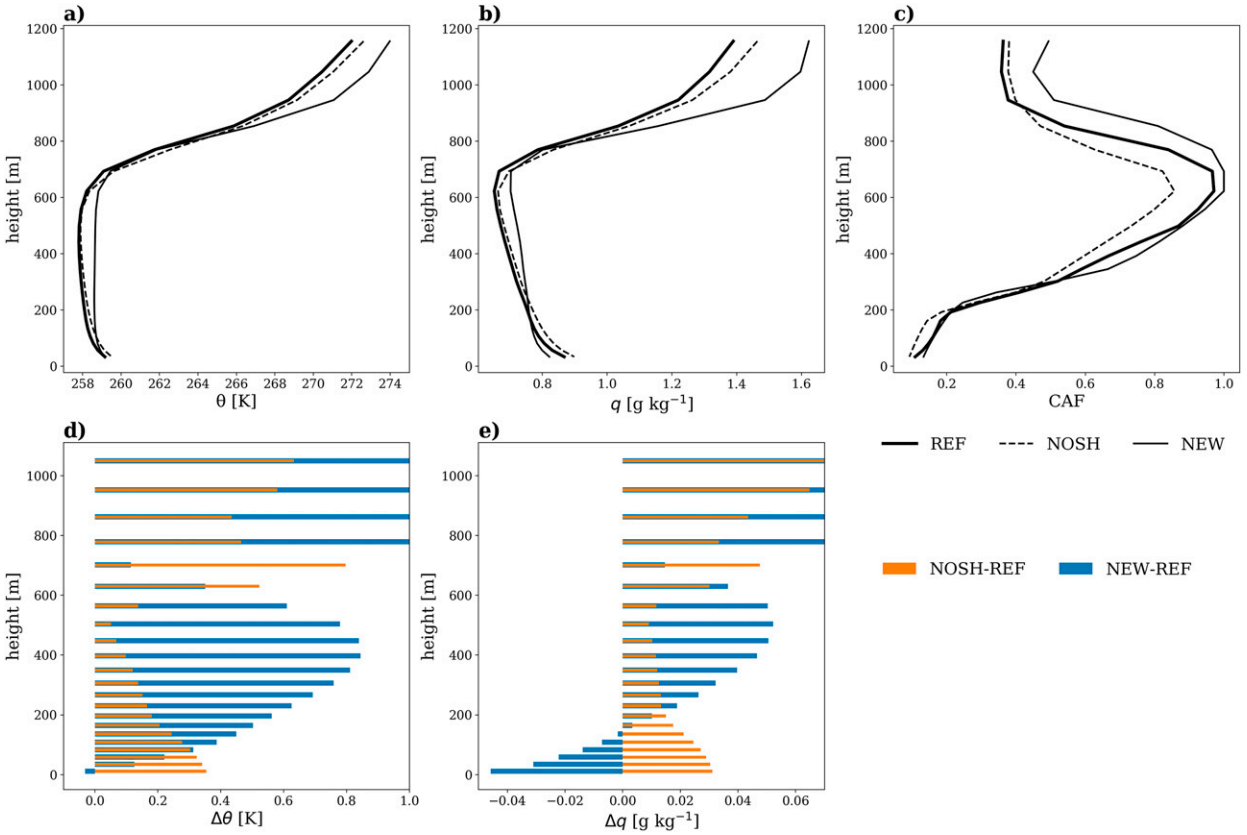

FIG. 6. Spatially averaged profiles within the stratocumulus ROI (ROI 1) of (a) potential temperature (K), (b) specific humidity (g kg^{-1}), and (c) cloud area fraction (CAF). The line styles refer to different sensitivity runs: REF (solid, thick), NOSH (dashed, thin), and NEW (solid, thin). Differences between the averaged profiles of (d) potential temperature, and (e) specific humidity between NOSH and REF (orange) and NEW and REF (blue).

lowest 200 m of the atmosphere, a significant cooling. At heights of about 200–300 m, a transition from negative to positive values, and thus from cooling to warming contributions of the scheme, occurs. From there upward, the shallow convection scheme warms the PBL at rates up to 3 K h^{-1}. Both cooling and warming result from the updrafts, which transport heat away from the surface and release it higher in the PBL. In the deep convective PBL type, only dry updrafts occur (Fig. 2, type V) leading to the abrupt cessation of δT^{sc} values around the cloud base height (~1500 m). Occasional values of δT^{sc} that differ from 0 K h^{-1} inside the cloud layer within the deep convective PBL indicate a variation of PBL type during the accumulation interval of the tendency output (section 2b).

The two tendencies δT^{turb} and δT^{sc} can be combined into an EDMF tendency δT^{EDMF} (Fig. 5f). Throughout the boundary layer depth, δT^{EDMF} exhibits nearly constant vertical profiles of 1–3 K h^{-1} with a maximum of over 5 K h^{-1} near the sea ice edge. These constant EDMF profiles imply a compensation between the strong positive and negative contributions of δT^{turb} and δT^{sc} near the surface, while at higher levels, the positive contributions of both tendencies complement each other. For example, the transition from negative to positive values in δT^{sc} (Fig. 5e) between 200 and 300 m is not noticeable in δT^{EDMF}, because δT^{turb} decreases simultaneously (Fig. 5d). This decrease in δT^{turb} originates from the reduced vertical temperature gradients due to the warming of the shallow convection scheme. This interplay leads to a nearly constant δT^{EDMF} with height.

In summary, the individual tendency output reveals that $\delta T^{\mathrm{micro}}$, δT^{turb}, and δT^{sc} are the most influential tendencies along the mCAO cross-section. The δT^{turb} and δT^{sc} strongly interact by compensating or complementing each other, forming the near-constant δT^{EDMF} with height. Furthermore, the contributions of δT^{EDMF} and $\delta T^{\mathrm{micro}}$ also compensate each other to a certain degree, especially in the deep convective PBL. These compensations between tendencies pose the question of how AROME-Arctic reacts to a change in its model physics configuration.

c. *Sensitivity experiments*

As shown above, tendency output from individual parameterization schemes reveals their compensating interplay within the mCAO, modulated by the diagnosed boundary layer types. Both of these aspects are now modified within the two sensitivity experiments, NOSH and NEW, described in section 2d.

We focus on two regions of interest (ROI, Fig. 4c), each covering an area of 40 × 40 grid points within a specific PBL type. ROI 1 ("stratocumulus" ROI) is located in the stratocumulus PBL type in both REF and NOSH. Large changes are

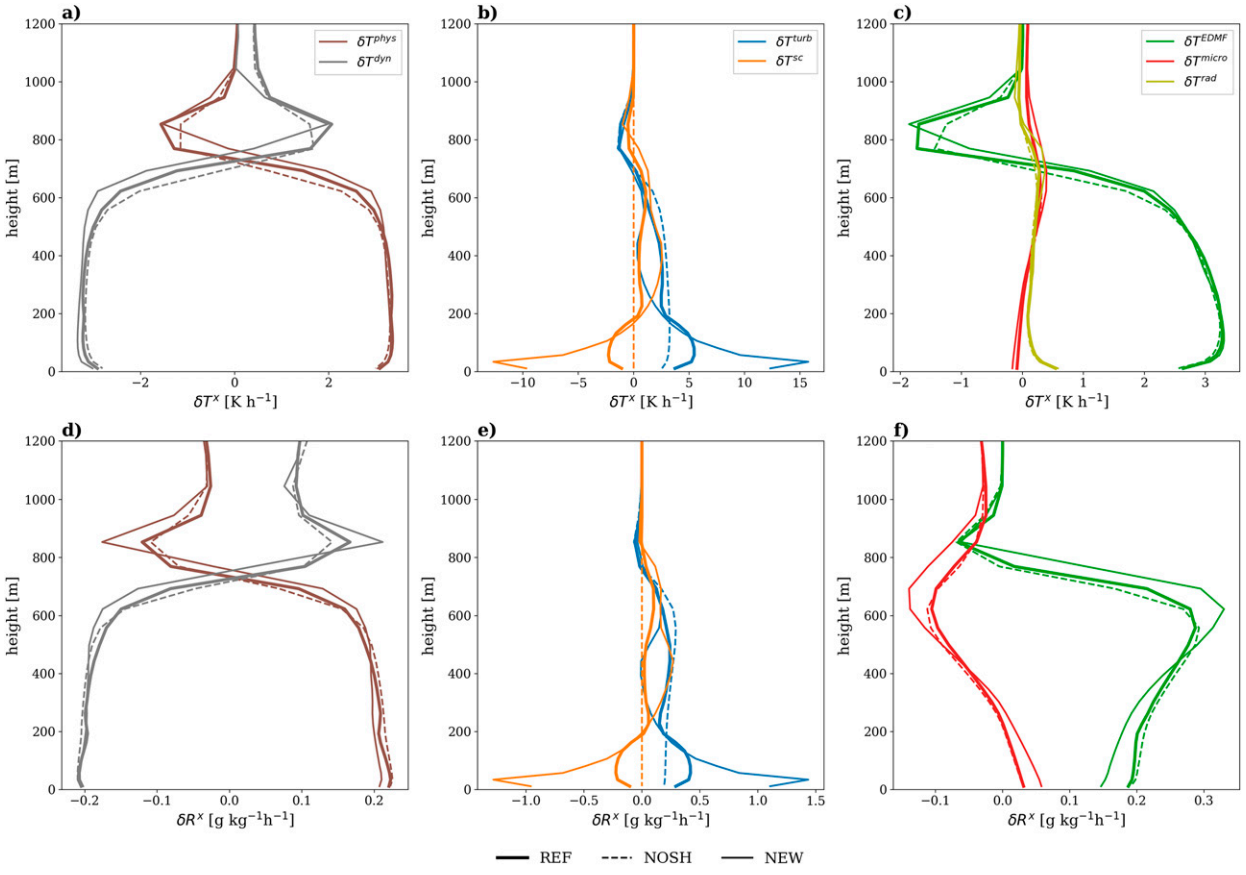

FIG. 7. Spatially averaged tendency profiles for the stratocumulus ROI (ROI 1). (a)–(c) Temperature tendencies (K h^{-1}) and (d)–(f) specific humidity tendencies (g kg^{-1} h^{-1}). The line colors denote different tendencies, physical (brown), dynamical (gray), turbulence (blue), shallow convection (orange), EDMF (green), microphysics (red), and radiation (yellow).

expected in NEW here because the stratocumulus PBL type is replaced by the shallow cumulus type. ROI 2 ("roll cloud" ROI) is located downstream of the mCAO (Fig. 3c). In this ROI, resolved convective motions are active in conjunction with parameterized shallow convection. Thus, the shallow convection scheme, which has been modified in both NOSH and NEW, plays a key role in ROI 2. For the sensitivity analysis within each ROI, averaged vertical profiles of selected variables and all major contributing tendencies for temperature and specific humidity are presented. For completeness, a brief analysis of two other ROIs, located in the stable and deep convective PBL type, can be found in the online supplemental material.

1) IMPACTS WITHIN THE STRATOCUMULUS ROI (ROI 1)

The averaged profiles of potential temperature depict a strong inversion in ROI 1 above 700 m at the same height in all three runs (Fig. 6a). While REF (solid, thick) and NOSH (dashed, thin) exhibit similar temperature and humidity profiles (Fig. 6b), NEW (solid, thin) exhibits more well-mixed atmospheric profiles throughout the PBL and a stronger inversion. Better preservation of atmospheric inversions is an expected result of the modified turbulence scheme in NEW.

The strong inversion in all runs is accompanied by stratocumulus-type clouds that spread from around 400 to 1000 m, with a maximum CAF around 600 m (Fig. 6c). NOSH exhibits the least cloud cover, and the thickest clouds are present in NEW.

The differences between the profiles in potential temperature and specific humidity of REF and NEW (Figs. 6d,e, blue) show a seamless transition from negative to positive differences in the lowest 600 m, confirming a more well-mixed PBL in NEW. The differences between NOSH and REF (orange) indicate a less well-mixed PBL in NOSH compared to REF. The lowest 200 m exhibit the largest differences, approaching 0.4 K (0.03 g kg^{-1}) and are collocated with the differences between shallow convection tendencies (see below).

Next, we investigate the tendencies of temperature and humidity in ROI 1 (Fig. 7). In all model runs, δT^{phys} and δR^{phys} are both positive from the surface through the middle of the cloud layer (600 m), reflecting net warming and moistening by the model physics (Figs. 7a,d). The tendencies δT^{dyn} and δR^{dyn} instead exhibit negative values in that layer. At heights between 700 and 1000 m, this relationship reverses due to cloud-top entrainment. Colder and drier air from within the PBL is

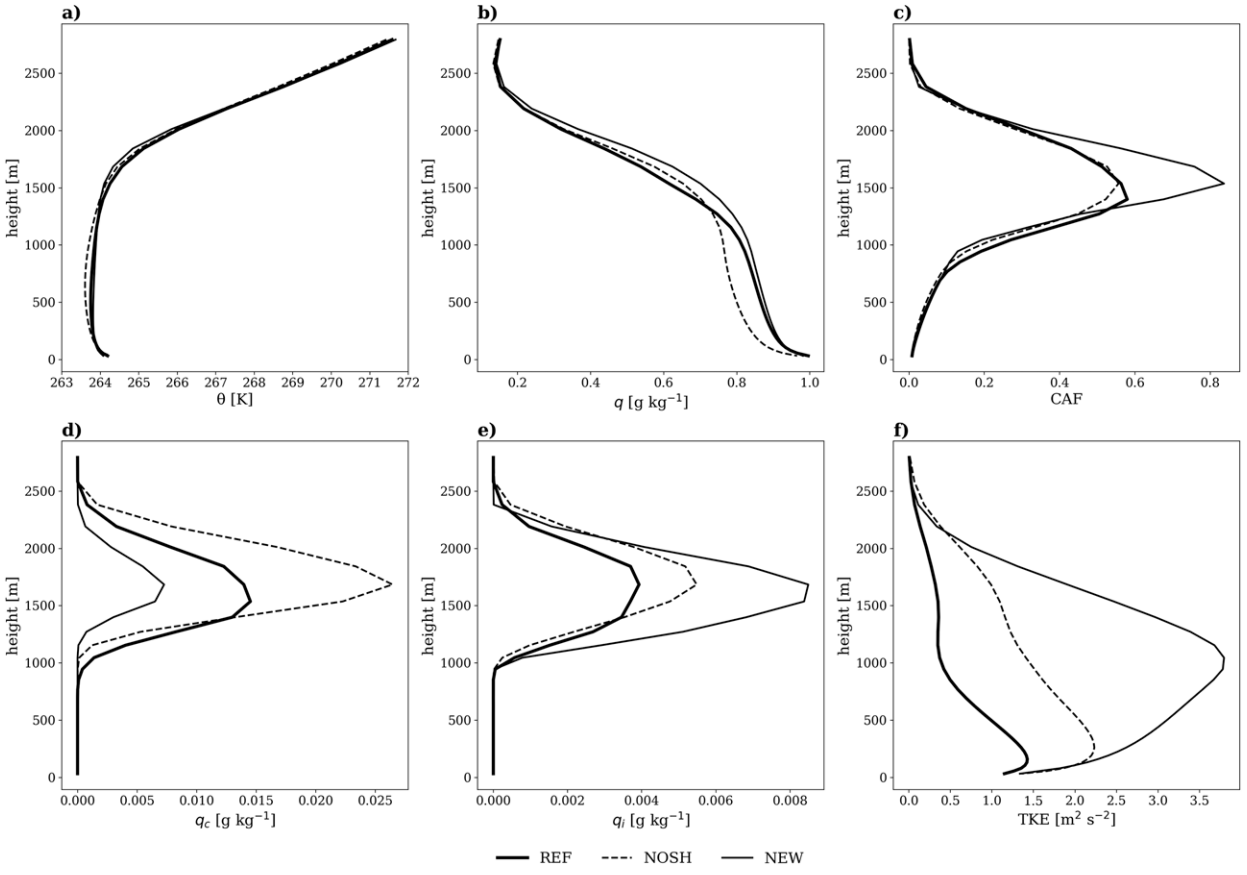

FIG. 8. Spatially averaged profiles within the roll cloud ROI (ROI 2) of (a) potential temperature (K), (b) specific humidity (g kg^{-1}), (c) cloud area fraction (CAF), (d) cloud water (g kg^{-1}), (e) cloud ice (g kg^{-1}), and (f) TKE (m^{-2} s^{-2}). The line styles refer to different sensitivity runs: REF (solid, thick), NOSH (dashed, thin), and NEW (solid, thin).

mixed upward into the inversion, substantiated by the negative contributions of δT^{turb}, δT^{sc}, δR^{turb}, and δR^{sc} (Figs. 7b,e). Meanwhile, warmer and more moist air is advected into the ROI at these heights. It is apparent that the physical and dynamical tendencies closely compensate each other in all runs.

Much larger sensitivities are found for δT^{turb} and δR^{turb}, as well as for δT^{sc} and δR^{sc} (Figs. 7b,e). In REF and NEW, δT^{sc} and δR^{sc} are both negative near the surface, but at varying magnitudes. In REF, these tendencies reach values of $-2\,\text{K}\,\text{h}^{-1}$ and $-0.1\,\text{g}\,\text{kg}^{-1}\,\text{h}^{-1}$, respectively, and exhibit an almost constant contribution below cloud base and within cloud layers (Fig. 6c). In comparison, δT^{turb} and δR^{turb} exhibit a similar shape, but reach higher absolute values of up to $5\,\text{K}\,\text{h}^{-1}$ ($0.4\,\text{g}\,\text{kg}^{-1}\,\text{h}^{-1}$). In NOSH, δT^{turb} and δR^{turb} instead exhibit near constant values of about $3\,\text{K}\,\text{h}^{-1}$ and $0.22\,\text{g}\,\text{kg}^{-1}\,\text{h}^{-1}$, respectively, for the lowest 600 m. Thus, the turbulence scheme consistently warms and moistens the lower PBL.

In NEW, contributions from the shallow convection scheme (δT^{sc} and δR^{sc}) reach values of $-12\,\text{K}\,\text{h}^{-1}$ and $-1\,\text{g}\,\text{kg}^{-1}\,\text{h}^{-1}$ near the surface, exceeding the tendencies in REF and NOSH by up to an order of magnitude. These strongly negative contributions below cloud base transition to positive contributions within the clouds (Fig. 6c). Contributions from the turbulence scheme (δT^{turb} and δR^{turb}, Figs. 7b,e) oppose that from the shallow convection scheme, showing large positive values near the surface that diminish with height. Thus, the shallow convection scheme in NEW contributes most to vertical mixing inside the cloud layer in ROI 1, opposite REF and NOSH, in which the turbulence scheme dominates the mixing process.

While each sensitivity experiment shows a distinct response in the contributions from the turbulence and the shallow convection schemes, the resulting δT^{EDMF} and δR^{EDMF} (Table 1) remain nearly unchanged between the runs (Figs. 7c,f, green). The similar EDMF profiles again underline the compensation between the turbulence and the shallow convection schemes. The biggest change is seen for δR^{EDMF} in NEW, as it exhibits a stronger gradient in the lowest 700 m. This gradient, however, is compensated by δR^{micro}, which is negatively correlated with δR^{EDMF}. In the end, this plethora of compensating tendencies results in the nearly unchanged δT^{phys} and δR^{phys} for ROI 1 between the different model runs (Figs. 7a,d). Furthermore, the unchanging EDMF tendencies in NOSH demonstrate that the role of the shallow convection scheme is taken over by the turbulence scheme in ROI 1.

Thus, neither replacing the stratocumulus with the shallow cumulus PBL type, as in NEW, nor removing the contribution

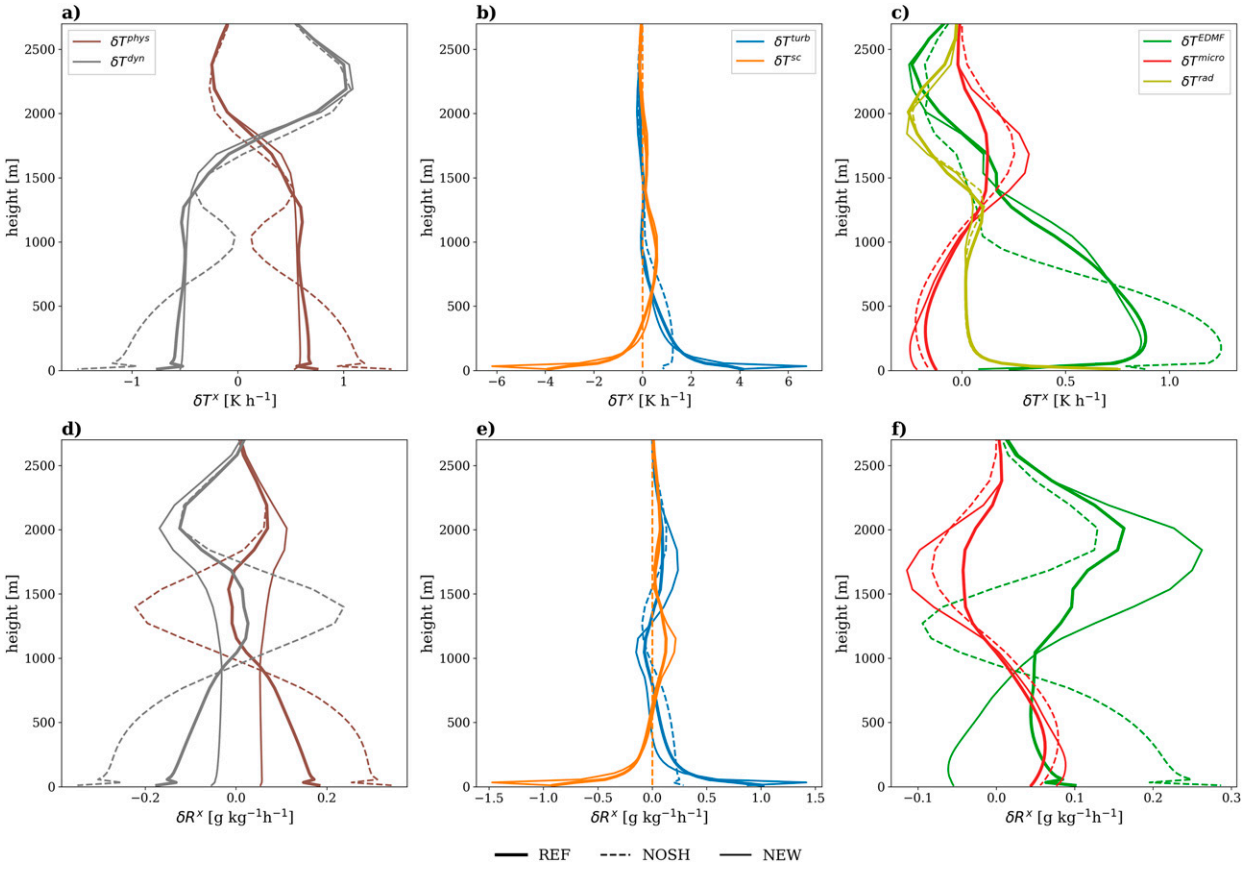

FIG. 9. Spatially averaged tendency profiles for the roll cloud ROI (ROI 2). (a)–(c) Temperature tendencies (K h^{-1}) and (d)–(f) specific humidity tendencies (g kg^{-1} h^{-1}). The line colors denote different tendencies, physical (brown), dynamical (gray), turbulence (blue), shallow convection (orange), EDMF (green), microphysics (red), and radiation (yellow).

from the shallow convection scheme, as in NOSH, results in substantial changes in either the temperature or specific humidity profiles in ROI 1, although the individual tendencies are substantially different in each simulation. One notable impact of the large contribution of the shallow convection scheme in NEW is that it yields the most well-mixed PBL of all runs (Figs. 6a,b). Furthermore, the differences between the temperature and specific humidity profiles (Figs. 6d,e) are collocated with differences between the respective contributions of the shallow convection scheme (Figs. 7b,e). Therefore, the individual tendencies allow us to decipher process-related differences between the model runs.

2) IMPACTS WITHIN THE ROLL CLOUD ROI (ROI 2)

Within the roll cloud ROI (ROI 2), the PBL and the cloud layer extend to about 2000 m. In REF, the temperature and humidity profiles are mostly between the profiles in NOSH and NEW (Figs. 8a,b). NOSH exhibits the least well-mixed profiles, while NEW, again, exhibits the most well-mixed profiles. The boundary layer clouds in all runs are located between 1000 and 2000 m (Fig. 8c). NEW again exhibits the most cloud cover, followed by REF and NOSH.

The modeled cloud condensate is quite sensitive to parameterization changes (Figs. 8d,e). REF shows mixed-phase clouds with a higher cloud water content (0.015 g kg^{-1}) than cloud ice content (0.004 g kg^{-1}). NOSH likewise exhibits mixed-phased clouds with the highest concentration of condensate, despite the lowest cloud fraction. The mass fraction of cloud water is nearly doubled (0.026 g kg^{-1}) in NOSH compared to REF. NEW, in contrast, exhibits the lowest amount of cloud water and the highest amount of cloud ice (0.0085 g kg^{-1}).

Substantial differences in TKE between the runs also occur (Fig. 8f). Both sensitivity runs depict higher values throughout the PBL compared to REF. NOSH has a nearly constant offset from REF above the lowest 150 m throughout the PBL. NEW has the highest TKE values of all runs, which continuously increase through cloud base (Fig. 8c). In NOSH, the less stable PBL causes increased buoyancy and shear production of TKE. In NEW, the increased values of TKE are the result of the addition of the energy cascade term to the TKE budget (DR21). This new source term enhances TKE in the upper half of the subcloud layer, thereby enhancing the turbulent transport between the subcloud and cloud layers.

The clearest impression of the model's response in the different simulations is given by δR^{dyn} (Fig. 9a, gray). In REF (solid, thick), δR^{dyn} is negative near the surface and below cloud base, indicating a drying contribution from the model dynamics. Meanwhile, the cloud layers (Fig. 8c) are moistened by the model dynamics, demonstrated by the positive values of

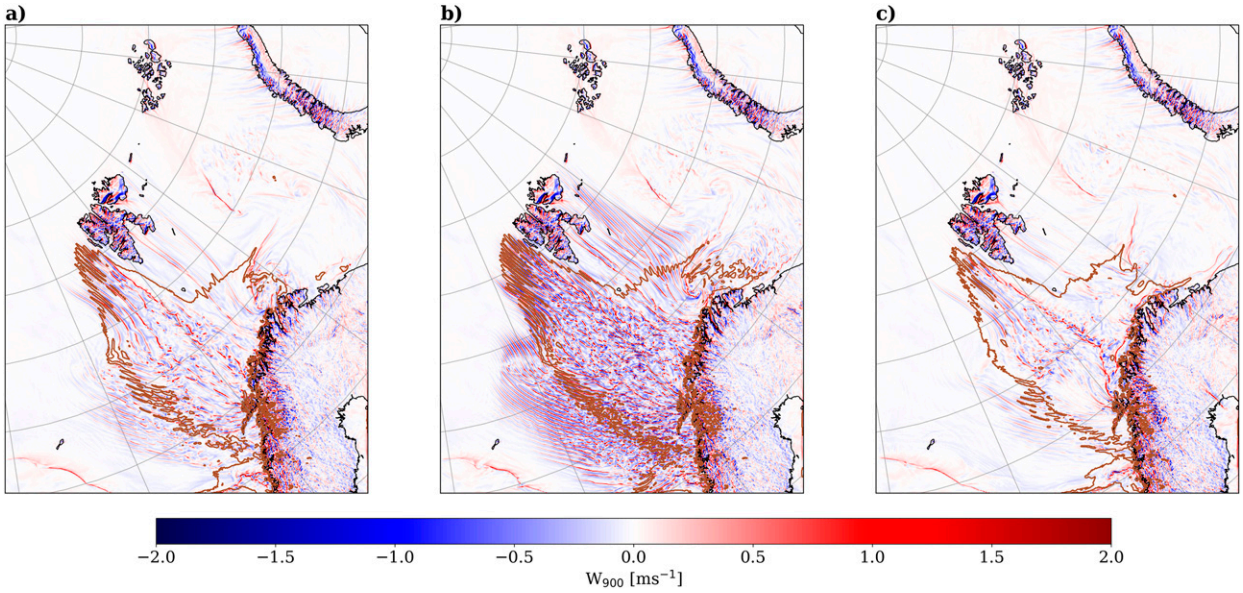

FIG. 10. Instantaneous vertical velocity (m s^{-1}) at 900 hPa valid at 1200 UTC 26 Dec 2015 for (a) REF, (b) NOSH, and (c) NEW. The brown contour depicts the onset of the deep convective PBL type in each experiment.

δR^{dyn}, similar to the shallow convection scheme. In NOSH (dashed), this resemblance is even more distinct. In contrast, such behavior is absent in NEW (solid, thin), in which δR^{dyn} shows a small, nearly constant negative contribution throughout the lowest 1700 m. Thus, the more or less active shallow convection scheme triggers a dynamical response of the model within the roll cloud ROI.

The EDMF tendency shows similar changes regarding the strength of the shallow convection scheme, exemplified here by δR^{EDMF} (Fig. 9f, green). Near the surface, there is a drying in NEW, whereas in REF and NOSH there is moistening. Tendencies in NOSH are more than twice as large as those in REF. In contrast to the other two simulations, NOSH exhibits a local minimum in δR^{EDMF} between 1000 and 1500 m before reaching a maximum around 2000 m. This local minimum coincides with the local maximum of δR^{dyn} in NOSH (Fig. 8d, gray, dashed), indicating that the air mixed upward by the parameterization is drier than the surrounding air. Thus, the vertical transport in NOSH is mostly done by the model dynamics on the grid-scale and not by the EDMF-framework, only represented by the turbulence scheme, on the subgrid-scale.

It thus appears that the turbulence scheme in NOSH is not able to compensate entirely for the missing shallow convection scheme in the roll cloud ROI, in contrast to the stratocumulus ROI (Figs. 7c,f). In turn, we find a strong dynamical response in NOSH that transports heat and moisture from near the surface to the subcloud and cloud layers (Fig. 9a), similar to a shallow convection scheme. With increasing strength of the shallow convection scheme, such a response is smaller in REF, and is largely absent in NEW.

d. Interaction of grid-scale and subgrid-scale processes

The dynamical responses of the model revealed above can be expected to be linked to the ratio between parameterized and resolved vertical transport in the PBL. Shallow convection mainly represents the parameterized transport while the grid-scale vertical velocity represents the resolved transport. We therefore investigate simulated vertical velocities, focusing on the 900-hPa level (Fig. 10).

Apart from orographic effects, only areas affected by the mCAO show strong vertical velocities in all simulations. REF primarily exhibits resolved vertical velocities within the deep convective PBL type (brown contour), but also farther south, including ROI 2. NOSH exhibits much stronger and widespread vertical velocities, which frequently exceed 2 m s^{-1}. Long bands of alternating updrafts and downdrafts can be seen, resembling convective rolls that often occur during an mCAO (Etling and Brown 1993). Farther south, near the Norwegian coast, these organized rolls break into cellular structures. While NEW depicts an overall reduction in vertical velocities, values of up to 2 m s^{-1} are present in the deep convective PBL type. The deep convective PBL appears distinct, as all vertical motions in the cloud layer must be resolved by the model. Nonetheless, the resolved convection in the deep convective PBL type in NEW is weaker than in REF. This indicates that the increased parameterized shallow convection until cloud base (see Fig. 2, type V), accompanied by a more well-mixed subcloud layer (Figs. 8a,b), reduces the buildup of intense resolved convection in NEW, otherwise present in REF. Hence, the response of the dynamical tendencies of NOSH and NEW (Figs. 9a,d) is manifested by the presence or absence of grid-scale updrafts.

Such pronounced changes in resolved vertical velocities can impact several other simulated quantities, regarding boundary layer clouds and their morphology, which enables a comparison with satellite imagery (Fig. 11). The satellite image (Fig. 11a) depicts cloud streets forming immediately downstream of the sea ice edge that transition into cellular convection around the latitude of Jan Mayen (see Fig. 1).

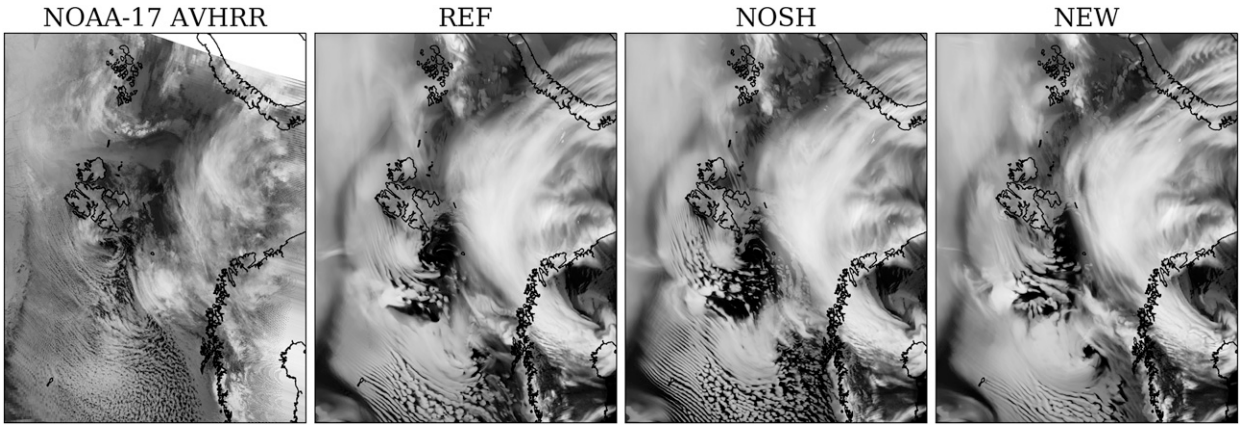

FIG. 11. (a) Infrared (channel 4) satellite image from the *NOAA-17* AVHRR instrument at 1935 UTC 25 Dec 2015. Outgoing longwave radiation (OLR) at the top of the atmosphere (TOA) in (b) REF, (c) NOSH, and (d) NEW at 1900 UTC 25 Dec 2015. Jan Mayen is the island in the bottom left.

In contrast to the satellite image, REF (Fig. 11b) only shows rudimentary cloud streets west of Svalbard and around Jan Mayen, which are often superimposed with stratiform clouds. Farther downstream, in good agreement with the observations, the cloud streets break into closed cells which, however, exceed the spatial extent of the observed convective cells. NOSH (Fig. 11c) depicts distinct cloud streets in close proximity to the sea ice edge, which break into smaller and more numerous individual cells than in REF. NOSH also produces cloud structures larger than those in the satellite image. Finally, NEW (Fig. 11d) displays the greatest cloud cover, with stratocumulus type clouds covering most of the mCAO. Cloud streets are barely visible south of Jan Mayen, and there is no breakup into single cells.

Thus, the changes to the shallow convection scheme in NOSH and NEW lead to a different partitioning of resolved and parameterized convection. As a result, substantial changes in vertical wind velocities emerge (Fig. 10), which in turn affect the representation of cloud condensates (Figs. 8d,e) and cloud morphology (Fig. 11) in AROME-Arctic.

4. Discussion

Individual tendency output has been utilized in this study to identify the governing parameterized processes and their interplay in an Arctic mCAO. Four aspects of the presented findings deserve a more detailed discussion, following below.

a. The role of model-internal boundary layer types

As revealed by ROI 1, PBL types can strongly modulate the interactions of individual parameterization schemes. The consideration of PBL types enables a more robust comparison of individual tendencies between different model runs because they inform about boundary conditions imposed on some schemes. PBL types are also commonly used in other NWP models, as they enable an adjustment of specific schemes to a wide range of different atmospheric situations, such as cloud-free nights, shallow cumulus convection, or, in our case, an mCAO. In the Integrated Forecast System model, for example, PBL types determine the use of the shallow convection or deep convection scheme (ECMWF 2013). It seems advisable that such model-internal PBL types be added as model output and be taken into account when investigating tendencies contributed by individual parameterizations.

b. The interplay of compensating parameterization schemes

The strong anticorrelation between the tendencies contributed by the turbulence and the shallow convection schemes is a central finding in our study (cf. Figs. 5, 7, 9). The turbulence scheme mixes locally down the gradient, whereas the shallow convection scheme acts nonlocally and draws its kinetic energy from buoyant production in the lower boundary layer (Lenderink and Holtslag 2004). Effectively, shallow convection transports heat and moisture away from the surface, thereby cooling and drying near-surface model levels. The turbulence scheme compensates for this effect by mixing heat and moisture from the surface upward down the vertical gradient.

Compensating behavior is also evident between the EDMF and microphysics, and the physical and dynamical tendencies in the convective boundary layer. The corresponding interplay was also found for several other NWP models (Niemelä and Fortelius 2005; Tomassini et al. 2017; Kim et al. 2018). Often only small residual terms remain from the very strong, opposing individual tendencies. This poses the question of whether such strong compensations could induce unwanted side effects. Regarding the common practice of model tuning, one can envision a scenario in which the contribution of parameterization scheme A is artificially enhanced, only because its contribution is constantly counteracted by another parameterization scheme. Such a condition could potentially hamper mid- and long-term model development.

Despite this compensation, the individual tendencies allow us to decipher process-related differences between the model runs. In ROI 1, the modeled profiles of temperature and specific humidity are different between the model runs (Figs. 6d,e). Both the warmer and more moist near-surface layer (200 m) in NOSH, as well as the better ventilation of the lowest 600 m in NEW are owing to differences in the shallow

convection scheme (Figs. 7b,e). Thus, individual tendencies aid in understanding differences between grid-scale atmospheric temperature or humidity profiles. Combining such analyses with observations, the tendency output could help to identify process-related errors within NWP models.

c. *Interacting subgrid- and grid-scale vertical transport*

The sensitivity experiments NOSH and NEW lead to opposite dynamical responses of the model, evidenced by the presence or absence of resolved vertical velocities (Fig. 10). These grid-scale updrafts indicate whether the EDMF framework fully accounts for the vertical mixing in the boundary layer (Figs. 7c,f) or not (Figs. 9c,f). NOSH enhances these grid-scale up- and downdrafts, while NEW largely suppresses them. Similar results were found in an LES study by Honnert et al. (2011), where the authors document an over and underestimation of resolved vertical motion in the respective absence or presence of a mass-flux scheme.

As demonstrated in this study, the relative strength of resolved versus parameterized convective transport depends on the convection scheme. The microphysics and the dynamical core, especially the strength of the horizontal diffusion, can also play a key role, however (Field et al. 2017). Downdrafts and cold pool mesoscale circulations originate from the evaporation of rain or snow and the associated cooling of the atmosphere. The setting LTOTPREC (see section 2a), used in all of our simulations, forwards the precipitation produced in the shallow convection scheme to the grid-scale condensates, used again by the microphysics. Thereby, LTOTPREC might act as a first step to establish a transfer from the parameterized to the resolved scales.

Clearly, the mCAO studied here differs substantially from other convective regimes, such as land-based, subgrid-scale shallow cumulus convection (e.g., Brown et al. 2002). During such regimes, the shallow convection scheme is essential for the convective transport. DR21, for example, note substantial drying of the subcloud layer by convection, captured better by NEW compared to REF. Herein lies a potential caveat for further model development: If one improves the model's performance for subgrid-scale shallow cumulus convection by increasing the parameterized, convective transport, one might simultaneously increase the need to reduce this convective transport during events that include partially resolved convection, such as the mCAO studied here.

d. *Change in cloud condensates*

The shift from liquid to ice condensates in NEW is unwanted (Figs. 8e,d). Arctic forecasts often suffer from an underrepresentation of supercooled liquid and mixed-phase clouds, while introducing ice condensates too frequently (Morrison et al. 2012; Engdahl et al. 2020). In our case study, the increase in ice condensates in NEW is connected to the treatment of resolved versus parameterized vertical motions. In regions over the open ocean and affected by the mCAO, cloud water only occurs in clouds that are directly fed by grid-scale vertical updrafts. In contrast, clouds that are solely fed by subgrid updrafts in REF and NEW consist of ice only. Thus, the absence of grid-scale updrafts in NEW (Fig. 10c) leads to the observed increase in cloud ice. In the same manner, the increase in cloud water in NOSH can be related to the more numerous grid-scale updrafts in that run. The mechanisms behind this shift in condensates together with the impact of the recent advancement in the microphysics scheme of AROME-Arctic, called ICE-T (Engdahl et al. 2020), will be investigated in a further study with the individual tendency output.

5. Conclusions and outlook

The simulation of an mCAO relies on the interplay of many parameterization schemes that contribute to forecast uncertainty, particularly in high latitudes. In this study, we demonstrated the utility of individual tendency output as a diagnostic tool in a regional, convection-permitting NWP model during a strong mCAO. We identify controlling factors for the activity of certain schemes, study the interplay between them, and investigate the model's subgrid adaption to changes in its physics package. We find that

- Analysis of individual tendencies strongly profits from considering modeled PBL types.
- Strong compensation between individual tendencies is prevalent. The same physical tendency for temperature and specific humidity may emerge from individual tendencies that can differ by up to an order of magnitude. Such compensating tendencies could lead to an artificial enhancement of individual schemes by model tuning and hamper model development.
- Despite similar physical tendencies for temperature and specific humidity, differences in atmospheric profiles do still occur. In the case studied here, these differences can be traced back to different individual tendencies. Future work could decipher the temporal development of the individual tendencies and their influence on atmospheric profiles, by enabling output at every single model time step.
- Considerable change in the interplay of individual tendencies and therefore in the resulting physical tendencies for temperature and specific humidity can be found when a dynamical response of the model is triggered by the sensitivity experiments. In our case study such a response can be identified by the presence or absence of grid-scale updrafts and downdrafts.
- In AROME-Arctic, clouds that are fed by resolved, grid-scale updrafts consist of both liquid and ice condensates, whereas clouds that are solely fed by parameterized updrafts consist of ice only. Therefore, the relationship between parameterized vertical transport, cloud morphology, and especially cloud condensates in AROME-Arctic should be more closely investigated.

Individual tendency output provides valuable insights into the workings of NWP models and helps to elaborate process-related changes to the model system. We agree with Lackmann and Thompson (2019) that many useful model fields provided by the physics routines, including individual tendencies, are often overlooked by the model community and advocate for a more widespread output and usage of such fields for continued model development.

Acknowledgments. We are very grateful for the constructive comments and insightful questions from the three anonymous reviewers that helped to substantially improve the manuscript. This work was funded by the Norwegian Research Council through the ALERTNESS project in the POLARPROG program (Project 280573).

Data availability statement. All model data that were created and used for this study are openly available from the THREDDS data server of the Norwegian Meteorological Institute (https://thredds.met.no/thredds/catalog/alertness/users/marvink/AMS_publication/catalog.html.).

REFERENCES

Abel, S. J., and Coauthors, 2017: The role of precipitation in controlling the transition from stratocumulus to cumulus clouds in a Northern Hemisphere cold-air outbreak. *J. Atmos. Sci.*, **74**, 2293–2314, https://doi.org/10.1175/JAS-D-16-0362.1.

Baas, P., S. R. de Roode, and G. Lenderink, 2008: The scaling behaviour of a turbulent kinetic energy closure model for stably stratified conditions. *Bound.-Layer Meteor.*, **127**, 17–36, https://doi.org/10.1007/s10546-007-9253-y.

Bechtold, P., J. W. M. Cuijpers, P. Mascart, and P. Trouilhet, 1995: Modeling of trade wind cumuli with a low-order turbulence model: Toward a unified description of Cu and Se clouds in meteorological models. *J. Atmos. Sci.*, **52**, 455–463, https://doi.org/10.1175/1520-0469(1995)052<0455:MOTWCW>2.0.CO;2.

Bengtsson, L., and Coauthors, 2017: The HARMONIE–AROME model configuration in the ALADIN–HIRLAM NWP system. *Mon. Wea. Rev.*, **145**, 1919–1935, https://doi.org/10.1175/MWR-D-16-0417.1.

Bougeault, P., 1982: Cloud-ensemble relations based on the gamma probability distribution for the higher-order models of the planetary boundary layer. *J. Atmos. Sci.*, **39**, 2691–2700, https://doi.org/10.1175/1520-0469(1982)039<2691:CERBOT>2.0.CO;2.

Brown, A. R., and Coauthors, 2002: Large-eddy simulation of the diurnal cycle of shallow cumulus convection over land. *Quart. J. Roy. Meteor. Soc.*, **128**, 1075–1093, https://doi.org/10.1256/003590002320373210.

Businger, S., and R. J. Reed, 1989: Cyclogenesis in cold air masses. *Wea. Forecasting*, **4**, 133–156, https://doi.org/10.1175/1520-0434(1989)004<0133:CICAM>2.0.CO;2.

de Rooy, W., and A. Siebesma, 2008: A simple parameterization for detrainment in shallow cumulus. *Mon. Wea. Rev.*, **136**, 560–576, https://doi.org/10.1175/2007MWR2201.1.

Deardorff, J. W., 1980: Stratocumulus-capped mixed layers derived from a three-dimensional model. *Bound.-Layer Meteor.*, **18**, 495–527, https://doi.org/10.1007/BF00119502.

ECMWF, 2013: IFS Documentation CY38R1—Part IV: Physical processes. No. 4, IFS Documentation CY38R1, ECMWF, https://doi.org/10.21957/vr0gh9gt9.

Engdahl, B. J. K., B. E. K. Nygaard, V. Losnedal, G. Thompson, and L. Bengtsson, 2020: Effects of the ICE-T microphysics scheme in HARMONIE–AROME on estimated ice loads on transmission lines. *Cold Reg. Sci. Technol.*, **179**, 103139, https://doi.org/10.1016/j.coldregions.2020.103139.

Etling, D., and R. A. Brown, 1993: Roll vortices in the planetary boundary layer: A review. *Bound.-Layer Meteor.*, **65**, 215–248, https://doi.org/10.1007/BF00705527.

Field, P. R., R. J. Cotton, K. McBeath, A. P. Lock, S. Webster, and R. P. Allan, 2014: Improving a convection-permitting model simulation of a cold air outbreak. *Quart. J. Roy. Meteor. Soc.*, **140**, 124–138, https://doi.org/10.1002/qj.2116.

——, and Coauthors, 2017: Exploring the convective grey zone with regional simulations of a cold air outbreak. *Quart. J. Roy. Meteor. Soc.*, **143**, 2537–2555, https://doi.org/10.1002/qj.3105.

Fouquart, Y., and B. Bonnel, 1980: Computations of solar heating of the Earth's atmosphere—A new parameterization. *Beitr. Phys. Atmos.*, **53**, 35–62.

Grossman, R. L., and A. K. Betts, 1990: Air–sea interaction during an extreme cold air outbreak from the eastern coast of the United States. *Mon. Wea. Rev.*, **118**, 324–342, https://doi.org/10.1175/1520-0493(1990)118<0324:AIDAEC>2.0.CO;2.

Hartmann, J., C. Kottmeier, and S. Raasch, 1997: Roll vortices and boundary-layer development during a cold air outbreak. *Bound.-Layer Meteor.*, **84**, 45–65, https://doi.org/10.1023/A:1000392931768.

Holloway, C. E., and Coauthors, 2014: Understanding and representing atmospheric convection across scales: Recommendations from the meeting held at Dartington Hall, Devon, UK, 28–30 January 2013. *Atmos. Sci. Lett.*, **15**, 348–353, https://doi.org/10.1002/asl2.508.

Honnert, R., V. Masson, and F. Couvreux, 2011: A diagnostic for evaluating the representation of turbulence in atmospheric models at the kilometric scale. *J. Atmos. Sci.*, **68**, 3112–3131, https://doi.org/10.1175/JAS-D-11-061.1.

Iwasaki, T., T. Shoji, Y. Kanno, M. Sawada, M. Ujiie, and K. Takaya, 2014: Isentropic analysis of polar cold airmass streams in the Northern Hemispheric winter. *J. Atmos. Sci.*, **71**, 2230–2243, https://doi.org/10.1175/JAS-D-13-058.1.

Joos, H., and H. Wernli, 2012: Influence of microphysical processes on the potential vorticity development in a warm conveyor belt: A case-study with the limited-area model COSMO. *Quart. J. Roy. Meteor. Soc.*, **138**, 407–418, https://doi.org/10.1002/qj.934.

Kim, J.-E.., C. Zhang, G. N. Kiladis, and P. Bechtold, 2018: Heating and moistening of the MJO during DYNAMO in ECMWF reforecasts. *J. Atmos. Sci.*, **75**, 1429–1452, https://doi.org/10.1175/JAS-D-17-0170.1.

Klein, S. A., and D. L. Hartmann, 1993: The seasonal cycle of low stratiform clouds. *J. Climate*, **6**, 1587–1606, https://doi.org/10.1175/1520-0442(1993)006<1587:TSCOLS>2.0.CO;2.

Lackmann, G. M., and G. Thompson, 2019: Hydrometeor lofting and mesoscale snowbands. *Mon. Wea. Rev.*, **147**, 3879–3899, https://doi.org/10.1175/MWR-D-19-0036.1.

Le Moigne, P., 2009: SURFEX scientific documentation. CNRM Tech. Rep., 211 pp.

Lenderink, G., and A. A. M. Holtslag, 2004: An updated length-scale formulation for turbulent mixing in clear and cloudy boundary layers. *Quart. J. Roy. Meteor. Soc.*, **130**, 3405–3427, https://doi.org/10.1256/qj.03.117.

Mlawer, E. J., S. J. Taubman, P. D. Brown, M. J. Iacono, and S. A. Clough, 1997: Radiative transfer for inhomogeneous atmospheres: RRTM, a validated correlated-k model for the longwave. *J. Geophys. Res.*, **102**, 16 663–16 682, https://doi.org/10.1029/97JD00237.

Morrison, H., G. de Boer, G. Feingold, J. Harrington, M. D. Shupe, and K. Sulia, 2012: Resilience of persistent Arctic mixed-phase clouds. *Nat. Geosci.*, **5**, 11–17, https://doi.org/10.1038/ngeo1332.

Müller, M., Y. Batrak, J. Kristiansen, M. Køltzow, G. Noer, and A. Korosov, 2017a: Characteristics of a convective-scale weather forecasting system for the European Arctic. *Mon. Wea. Rev.*, **145**, 4771–4787, https://doi.org/10.1175/MWR-D-17-0194.1.

——, and Coauthors, 2017b: AROME-MetCoOp: A Nordic convective-scale operational weather prediction model. *Wea. Forecasting*, **32**, 609–627, https://doi.org/10.1175/WAF-D-16-0099.1.

Neggers, R., 2009: A dual mass flux framework for boundary layer convection. Part II: Clouds., *J. Atmos. Sci.*, **66**, 1489–1506, https://doi.org/10.1175/2008JAS2636.1.

——, M. Köhler, and A. Beljaars, 2009: A dual mass flux framework for boundary layer convection. Part I: Transport. *J. Atmos. Sci.*, **66**, 1465–1487, https://doi.org/10.1175/2008JAS2635.1.

Niemelä, S., and C. Fortelius, 2005: Applicability of large-scale convection and condensation parameterization to meso-*y*-scale HIRLAM: A case study of a convective event. *Mon. Wea. Rev.*, **133**, 2422–2435, https://doi.org/10.1175/MWR2981.1.

Papritz, L., and S. Pfahl, 2016: Importance of latent heating in mesocyclones for the decay of cold air outbreaks: A numerical process study from the Pacific sector of the Southern Ocean. *Mon. Wea. Rev.*, **144**, 315–336, https://doi.org/10.1175/MWR-D-15-0268.1.

——, and H. Sodemann, 2018: Characterizing the local and intense water cycle during a cold air outbreak in the Nordic Seas. *Mon. Wea. Rev.*, **146**, 3567–3588, https://doi.org/10.1175/MWR-D-18-0172.1.

Samuelsen, E. M., and R. G. Graversen, 2019: Weather situation during observed ship-icing events off the coast of northern Norway and the Svalbard archipelago. *Wea. Climate Extremes*, **24**, 100200, https://doi.org/10.1016/j.wace.2019.100200.

Seity, Y., P. Brousseau, S. Malardel, G. Hello, P. Bénard, F. Bouttier, C. Lac, and V. Masson, 2011: The AROME-France convective-scale operational model. *Mon. Wea. Rev.*, **139**, 976–991, https://doi.org/10.1175/2010MWR3425.1.

Siebesma, A., P. Soares, and J. Teixeira, 2007: A combined eddy-diffusivity mass-flux approach for the convective boundary layer. *J. Atmos. Sci.*, **64**, 1230–1248, https://doi.org/10.1175/JAS3888.1.

Soares, P. M. M., P. M. A. Miranda, A. P. Siebesma, and J. Teixeira, 2004: An eddy-diffusivity/mass-flux parametrization for dry and shallow cumulus convection. *Quart. J. Roy. Meteor. Soc.*, **130**, 3365–3383, https://doi.org/10.1256/qj.03.223.

Stull, R. B., 1988: *An Introduction to Boundary Layer Meteorology*. Springer, 670 pp.

Tomassini, L., P. R. Field, R. Honnert, S. Malardel, R. McTaggart-Cowan, K. Saitou, A. T. Noda, and A. Seifert, 2017: The ''grey zone'' cold air outbreak global model intercomparison: A cross evaluation using large-eddy simulations. *J. Adv. Model. Earth Syst.*, **9**, 39–64, https://doi.org/10.1002/2016MS000822.

Vihma, T., and Coauthors, 2014: Advances in understanding and parameterization of small-scale physical processes in the marine Arctic climate system: A review. *Atmos. Chem. Phys.*, **14**, 9403–9450, https://doi.org/10.5194/acp-14-9403-2014.